The Astrophysical Journal, 954:51 (13pp), 2023 September 1 https://doi.org/10.3847/1538-4357/ace620

Seismic Signatures of the $^{12}C(\alpha, \gamma)^{16}O$ Reaction Rate in White Dwarf Models with Overshooting

Morgan T. Chidester, F. X. Timmes, and Ebraheem Farag
School of Earth and Space Exploration, Arizona State University, Tempe, AZ 85287, USA; taylormorgan32@gmail.com
Received 2023 April 7; revised 2023 June 22; accepted 2023 June 28; published 2023 August 22

Abstract

We consider the combined effects that overshooting and the $^{12}C(\alpha, \gamma)^{16}O$ reaction rate have on variable white dwarf (WD) stellar models. We find that carbon–oxygen (CO) WD models continue to yield pulsation signatures of the current experimental $^{12}C(\alpha, \gamma)^{16}O$ reaction rate probability distribution function when overshooting is included in the evolution. These signatures hold because the resonating mantle region, encompassing $\simeq 0.2\,M_\odot$ in a typical $\simeq 0.6\,M_\odot$ WD model, still undergoes radiative helium burning during the evolution to a WD. Our specific models show two potential low-order adiabatic g-modes, g_2 and g_6, that signalize the $^{12}C(\alpha, \gamma)^{16}O$ reaction rate probability distribution function. Both g-mode signatures induce average relative period shifts of $\Delta P/P = 0.44\%$ and $\Delta P/P = 1.33\%$ for g_2 and g_6, respectively. We find that g_6 is a trapped mode, and the g_2 period signature is inversely proportional to the $^{12}C(\alpha, \gamma)^{16}O$ reaction rate. The g_6 period signature generally separates the slower and faster reaction rates, and has a maximum relative period shift of $\Delta P/P = 3.45\%$. We conclude that low-order g-mode periods from CO WDs may still serve as viable probes for the $^{12}C(\alpha, \gamma)^{16}O$ reaction rate probability distribution function when overshooting is included in the evolution.

Unified Astronomy Thesaurus concepts: Asteroseismology (73); Nuclear astrophysics (1129); White dwarf stars (1799); Stellar physics (1621)

Supporting material: interactive figure

1. Introduction

Helium burning is primarily the fusion of helium into carbon by the triple-alpha (3α) process. All stars born with more than $\simeq 0.5\,M_\odot$ go through this stage of energy production as they evolve beyond the main sequence (e.g., Hansen et al. 2004). Helium burning also plays a key role in transients such as Type I X-ray bursts (Weinberg et al. 2006; Guichandut & Cumming 2023), Type Ia supernovae (Shen et al. 2018; Collins et al. 2022), and He-rich subdwarf O stars (Miller Bertolami et al. 2022; Werner et al. 2022). Helium burning also impacts several classes of distribution functions, such as the black hole mass distribution function (Fryer & Kalogera 2001; Sukhbold et al. 2018; Sajadian & Sahu 2023) including any mass gaps based on the pair-instability mechanism in the evolution of massive stars (Fowler & Hoyle 1964; Woosley et al. 2002; Farmer et al. 2019, 2020; Marchant & Moriya 2020; Renzo et al. 2020; Farag et al. 2022).

Helium burning is triggered by the 3α process releasing 7.5 MeV in fusion energy and producing ^{12}C (Hoyle 1954; Eriksen et al. 2020; Kibédi et al. 2020; Cook et al. 2021). This is a unique process, setting stringent conditions for helium ignition. The 3α process is followed by the α-capture reaction $^{12}C(\alpha, \gamma)^{16}O$, converting the ^{12}C into ^{16}O (deBoer et al. 2017; Mehta et al. 2022; Shen et al. 2023). These two isotopes are the principal products of helium burning. In addition, nearly all of a star's initial CNO abundances in the stellar interior are converted to ^{22}Ne at the onset of helium burning (Timmes et al. 2003; Howell et al. 2009; Bravo et al. 2010; Blondin et al. 2022; Meng et al. 2023). This marks the first time in a star's life where the core becomes neutron-rich. We follow the convention that ^{22}Ne is the "metallicity" of a carbon–oxygen (CO) white dwarf (WD).

The interiors of CO WDs are, in principle, the best probe of the ashes of helium burning. A goal of WD seismology is to characterize the chemical profiles of the principal products of helium burning (Metcalfe et al. 2001; Fontaine & Brassard 2002; Metcalfe et al. 2002; Metcalfe 2003; Straniero et al. 2003; De Gerónimo et al. 2017; Giammichele et al. 2017, 2018; Córsico et al. 2019; De Gerónimo et al. 2019; Córsico et al. 2022; Giammichele et al. 2022; Pepper et al. 2022; Romero et al. 2023) and the chemical profile of the trace ^{22}Ne metallicity (Camisassa et al. 2016; Giammichele et al. 2018; Chidester et al. 2021; Althaus & Córsico 2022).

Furthermore, regions within a CO WD model that burn helium radiatively during its prior evolution can offer potential constraints on the helium burning nuclear reaction rates. For example, Chidester et al. (2022, hereafter C22) found that certain trapped adiabatic g-modes in WD models may provide a pulsation signature that constrains the experimental $^{12}C(\alpha, \gamma)^{16}O$ reaction rate probability distribution function. These signature g-modes were shown to resonate with the region of the CO WD model that underwent radiative helium burning during its previous evolution. The innermost boundary of this resonant cavity corresponds to the molecular weight gradient at the O → C chemical transition, and the outermost boundary to the molecular weight C → He chemical transition. The resonating region encompasses $\simeq 0.2\,M_\odot$ of a typical $\simeq 0.6\,M_\odot$ WD model. C22 cautioned that the chemical structure and resulting pulsation spectrum is sensitive to the width of the O → C transition (Córsico et al. 2002; Salaris & Cassisi 2017; Pepper et al. 2022), the experimental 3α reaction rate probability distribution functions (deBoer et al. 2017; Kibédi et al. 2020; Schatz et al. 2022), convective boundary mixing

processes during core helium depletion (Salaris & Cassisi 2017; Anders et al. 2022), and the number of thermal pulses during the asymptotic giant branch (AGB) phase of evolution (De Gerónimo et al. 2017; Pepper et al. 2022).

Modeling convective boundary mixing processes at the convective–radiative interface during core helium burning (CHeb) in low- and intermediate-mass stellar models is currently uncertain (Herwig 2000; Salaris & Cassisi 2017; Anders et al. 2022; Jermyn et al. 2022; Blouin et al. 2023). Convective overshoot occurs because the convective boundary is not the location where convective velocities are zero, but the location where the buoyant acceleration of the fluid is zero. An order-of-magnitude expression, $\Delta x = u\Delta t$, provides an estimate for how far convective motions overshoot (Anders et al. 2022). Here, Δx is the overshoot distance, u is the convective velocity, and $\Delta t \simeq 1/N$, where N is the Brunt–Väisälä frequency in the stable region. There is disagreement on how to calculate Δx, but this estimate broadly shows $\Delta x \ll H_P$ in stellar environments, where H_P is the pressure scale height. The exponential overshoot parameterization (e.g., Herwig 2000) is frequently implemented in 1D models to describe this convective boundary mixing process, treating Δx as a free parameter. The values of Δx needed to match the gravity modes found in slowly pulsating B-type stars (Pedersen et al. 2021) suggest $\Delta x/H_P \simeq 0.1$, which is larger than 3D hydrodynamical simulations of low-Mach-number flows at stable interfaces indicate (Korre et al. 2019; Blouin et al. 2023).

The injection of fresh helium into the convective core enhances the rate of energy production by the ^{12}C $(\alpha, \gamma)^{16}$O reaction rate, increases the central ^{16}O mass fraction (e.g., De Gerónimo et al. 2017), and modifies the lifetime through this phase of evolution. The resulting increase in the radiative gradient can also lead to rapid growth in the convective helium core boundary (a "breathing pulse"). A consensus on breathing pulses being physical or numerical has not yet been reached (Caputo et al. 1989; Cassisi et al. 2003; Farmer et al. 2016; Constantino et al. 2017; Paxton et al. 2019).

C22 found a pulsation signature of the ^{12}C$(\alpha, \gamma)^{16}$O reaction rate probability distribution function using evolutionary models that purposely excluded overshooting. This article is novel in analyzing whether or not pulsation signals of the ^{12}C$(\alpha, \gamma)^{16}$O reaction rate probability distribution function still exist when overshooting at the inner convective–radiative interface during CHeB is included in the models' evolution history. Here, the inner convective–radiative interface is the transition from the convective core to the exterior radiative layer. Section 2 describes our models, Section 3 analyzes our models, Section 4 discusses our results, and we summarize our findings in Section 5. Appendix A lists the microphysics used, and Appendix B discusses variations with the number of isotopes in the reaction network and with the temporal resolution of our models.

2. Stellar Evolutionary Models

We define the term "model" to mean an evolutionary sequence that begins at the pre-main sequence, progresses through CHeB, and terminates as a cold WD. We define the term "snapshot" to mean a specific instance in time or phase of evolution within a model, and the term "set" to mean a suite of models or snapshots that have identical input physics except for the value of the ^{12}C$(\alpha, \gamma)^{16}$O reaction rate.

We use `MESA` version r15140 (Paxton et al. 2011, 2013, 2015, 2018, 2019; Jermyn et al. 2023) to build 2.1 $M_\odot$, $Z = 0.0151$ metallicity, $Y = 0.266$ He mass fraction, nonrotating models at the pre-main sequence. We adopt the AGSS09 (Asplund et al. 2009) abundances and use a 23-isotope nuclear reaction network, with ^{22}Ne being the heaviest isotope.[1] Our models employ `MESA`'s `Henyey` mixing-length theory (MLT) of convection option, with an MLT parameter of $\alpha = 1.5$. This is consistent with the value used in C22. We use the Ledoux criterion, and the predictive mixing scheme. Additional details of the `MESA` microphysics are listed in Appendix A.

As in C22, we span the current experimental ^{12}C$(\alpha, \gamma)^{16}$O reaction rate probability distribution function (deBoer et al. 2017; Mehta et al. 2022) from $\sigma = -3.0$ to $\sigma = +3.0$ in 0.5σ steps, totaling to 13 σ_i reaction rates; each model is prescribed one such σ_i ^{12}C$(\alpha, \gamma)^{16}$O reaction rate value for its evolution. We calculate one set of models without overshooting (NOV), and a second set with overshooting (OV) at the inner radiative–convective interface during the CHeB phase. Hence, each evolutionary model differs only in its σ_i ^{12}C$(\alpha, \gamma)^{16}$O reaction rate, and NOV or OV mixing prescription. This yields 26 individual stellar evolutionary models: 13 for the NOV set and 13 for the OV set. For $i = (-3.0, -2.5, \ldots, +2.5, +3.0)$, we use σ_i and $\sigma = i$ interchangeably to reference a given σ from the ^{12}C$(\alpha, \gamma)^{16}$O reaction rate probability distribution function.

After CHeB, the models evolve until $\log(L/L_\odot) = 3.0$, prior to the first thermal pulse on the AGB. At this snapshot, we interrupt the evolution of each model. All models at this snapshot thus have a C $\rightarrow$ He transition at nearly the same mass location. We use this snapshot to construct H-dominated atmosphere (DA) WDs by removing the hydrogen envelopes until $\log(M_{\rm H}/M_*) < -3.5$. The resulting composition profile structures are used to build 0.56 $M_\odot$ ab initio WD models with `wd_builder`, as done in C22. These WD models evolve until $T_{\rm eff} = 10{,}000$ K. We discuss the reasoning for constructing the WDs from the post-CHeB $\log(L/L_\odot) = 3.0$ snapshot in the following section.

We utilized version 6.0.1 of the `GYRE` code (Townsend & Teitler 2013; Townsend et al. 2018) to compute the adiabatic pulsations of our WD models throughout their respective cooling tracks (from ~50,000 to 10,000 K). We tracked the pulsations for the entire WD cooling track to observe the evolution of the adiabatic modes. Further, this was the most convenient way to auto-implement pulsation calculations for multiple models (i.e., we did not have to post-process the pulsation calculations over a specified $T_{\rm eff}$ range for each of the 26 models). We emphasize that the computed pulsations are adiabatic, and that the observed instability strip for DAV WDs spans only from ~13,000 to ~10,000 K. The inlist parameters were set to search for modes of harmonic degrees $\ell = 1, 2$ and radial orders $n \leqslant 25$, where our models were assumed to be nonrotating, hence only $m = 0$ azimuthal orders were present. For the adiabatic-mode analysis, we employed the fourth-order Gauss–Legendre collocation difference equation scheme (Iserles 1996; Townsend & Teitler 2013; Townsend et al. 2018).

Details of the `MESA` models and `GYRE` oscillation parameters are in the files to reproduce our results at doi:10.5281/zenodo.8126450.

[1] A comparison to a 30-isotope network is given in Appendix B.

2.1. Core Overshooting Prescription during the CHeB

During the CHeB phase, we use the following core overshooting parameters in the MESA inlist for the OV set:

```
! overshoot
min_overshoot_q=1d-3
overshoot_scheme(1)="exponential"
overshoot_zone_type(1)="any"
overshoot_zone_loc(1)="core"
overshoot_f(1)=0.016
overshoot_f0(1)=0.008
overshoot_mass_full_on(1)=0.01
overshoot_mass_full_off(1)=0.4.
```

Details of the specific parameters are described in the MESA documentation.[2] We choose the conventional Herwig (2000) value of `overshoot_f(1)=0.016`. This parameter sets the fractional distance of H_p to overshoot at the $\nabla_{\rm ad} = \nabla_{\rm rad}$ interface, for the order-of-magnitude estimate given in the introduction, $\Delta x = f_0 \cdot H_p$.

The trapped-mode seismic signatures found in C22 were resonating most with the region that underwent radiative helium burning, defined as R2. Their inner boundary of R2 is near the molecular weight gradient at the O → C transition (the "O drop") and their outer boundary is near the C → He transition. Mode trapping is sensitive to the location of both of these boundaries because they define the width of the resonant cavity.

One approach to analyzing the sensitivity of the R2 trapped-mode signatures is to fix one boundary and vary the other boundary. We fix the R2 outer boundary by excluding variations imposed from the thermal pulse history, hence the interruption at the post-CHeB $\log(L/L_\odot) = 3.0$ snapshot for all models. The phenomena that occur during the AGB phase is another source of model uncertainty. Gautschy (2023) found that early post-AGB pulsations can cause rapid growth of an instability that drives a super-wind which can shed much of the outer layers in a few years. Further, their 2.0 $M_\odot$, $Z = 0.02$ model shows a dynamic evolutionary track, especially during the AGB, that is similar to the models in this article. Gautschy (2023) summarizes that while the preliminary results show promise on future AGB and post-AGB phenomena, there are currently more questions than answers. We therefore leave the thermal pulse history and the particular envelope ejection phenomena on the AGB to future studies, and freeze the outermost R2 boundary before the first thermal pulse occurs. In this vein, we isolate the sensitivity of the R2 region to its inner boundary, and specifically address how core overshooting influences the pulsation signatures for the $^{12}C(\alpha, \gamma)^{16}O$ reaction rate probability distribution function.

We end this section by stating we are not advocating for a specific evolutionary model or overshooting scheme. Rather, we are exploring one approach to quantifying the coupled uncertainty between the $^{12}C(\alpha, \gamma)^{16}O$ reaction rate probability distribution function and a common overshooting model.

3. Results

3.1. Evolution of Composition Profiles

Figure 1 shows the mass fraction profiles for both sets at three evolutionary snapshots. The top row shows the mass fraction profiles for the NOV set, and the bottom row shows the mass fraction profiles for the OV set. The leftmost column shows the mass fraction profiles at the post-CHeB $\log(L/L_\odot) > 3.0$ snapshot. At this point, our models have not lost much mass and are all $\sim 2.1\, M_\odot$. The middle column shows the mass fraction profiles after removing the hydrogen envelopes until $\log(M_{\rm H}/M_*) < -3.5$. This snapshot shows the initial hot WD profiles, after completing one model step in `wd_builder`. The profiles shift slightly in mass location, but the overall composition structure only differs from the left panel in the thickness of the hydrogen envelope. The right column is the final snapshot of the mass fraction profiles, when the models reach $T_{\rm eff} = 10{,}000$ K. Diffusion was included on the WD cooling track and leads to the smoothness of the profiles in this column.

Figure 2 accentuates the differences between the NOV (top) and OV (bottom) mass fraction profiles for the final WD structures (right column of Figure 1). Here, we show the abundance in mass fraction with respect to fractional radius r/R. We partition the WDs' composition profiles into four regions: R1, R2, R3, and R4. This is similar to that done in C22. The regions are defined to estimate trapping (resonant) zones. Boundaries for mode trapping are typically near composition transitions because they generally have large mean molecular weight gradients. This may lead to partial reflections for a resonant mode(s), "trapping" it within the local cavity (Winget et al. 1981; Brassard et al. 1991). The Ledoux B profile (henceforth B) captures composition gradients and can estimate trapping regions. We use B as our primary guide to define the region boundaries for a given model. The R1–R2 boundary is set at the first local maximum in B that occurs after reaching peak ^{16}O in a given model's chemical profile. The R2–R3 boundary is set at the second local maximum in B. The R3–R4 boundary is set at the location where $X(^1H) > X(^4He)$.

In both NOV and OV sets, σ_i impacts the magnitudes of the ^{16}O and ^{12}C profiles in R1. Core overshooting changes the structure of these profiles, especially at $r/R \sim 0.37$, where the flatness of the profiles becomes disrupted. This is due to additional helium fuel ingested during CHeB, from overshooting and/or convection. The fuel ingestion from overshooting and convection is a coupled effect and specific to each σ_i model. After $r/R \sim 0.37$, there is some overlap in the profiles that perturbs the proportional trend with σ_i.

For both sets, the first group of vertical blue lines marks the R1–R2 boundary, with each line representing a given σ_i. The NOV set shows a steep composition gradient at the R1–R2 boundary, and the R1–R2 location is nearly the same for all σ_i. There is greater variance in the R1–R2 location for the OV set. Further, core overshooting has softened the ^{16}O and ^{12}C gradients, and the disruption of the profiles' regularity with σ_i continues into the start of the R2 region. At $r/R \sim 0.6$, the proportionality of σ_i to the ^{12}C and ^{16}O profiles is restored.

By design, from stopping at the first thermal pulse the R3 and R4 regions are almost identical between the NOV and OV sets. These regions are least affected from mixing processes in the core (e.g., overshooting).

In Figures 1 and 2, the OV chemical profiles show a nonconstant structure from overshooting during CHeB in the oxygen-dominated central core (below $\simeq 0.4\, M_\odot$). While element diffusion is included during the WD cooling phase, these chemical profiles may be further flattened by mixing processes not considered in this study such as time-dependent

[2] https://docs.mesastar.org/en/latest/

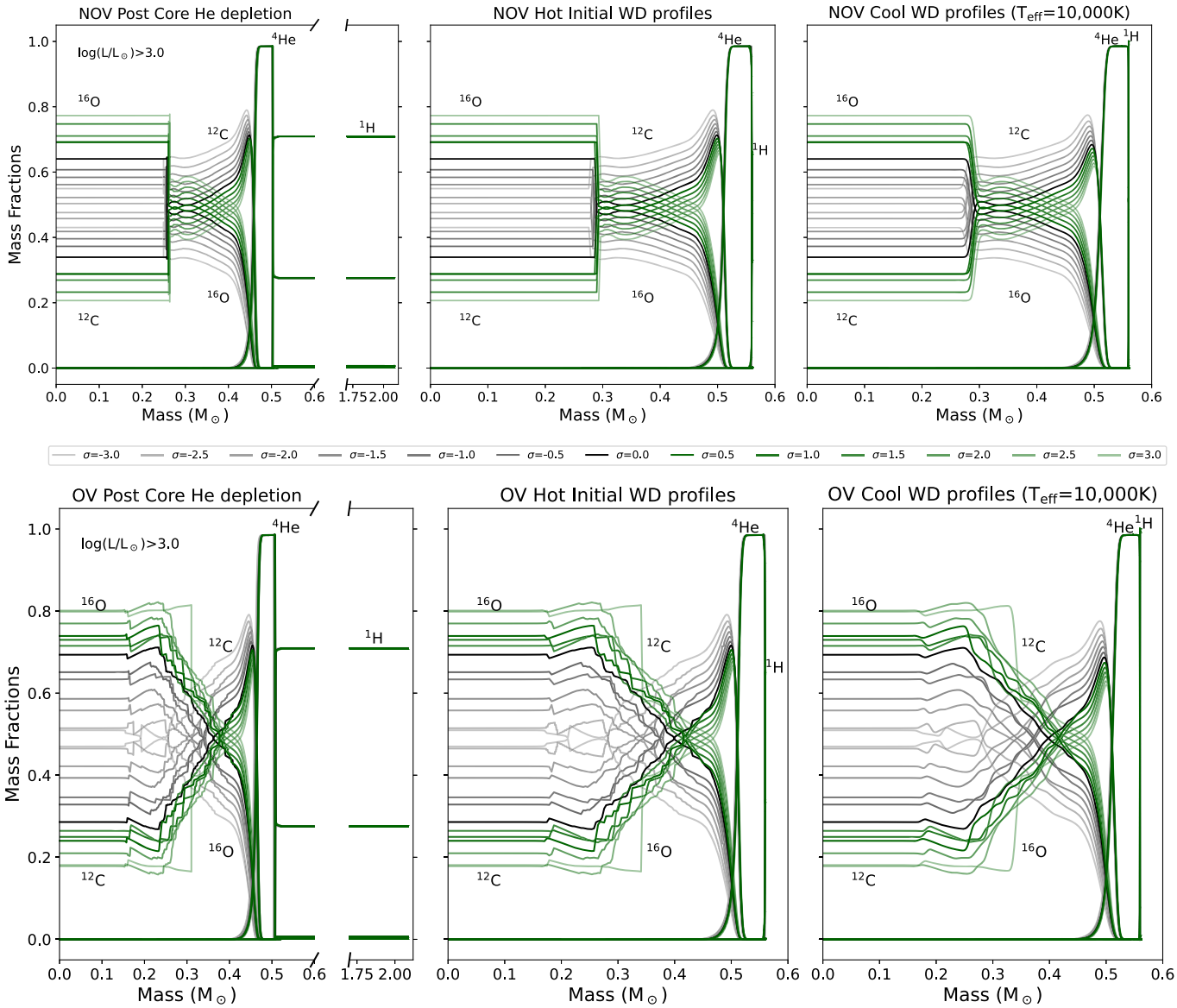

Figure 1. Top: mass fraction profiles without overshooting (NOV) during the CHeB phase. Left: mass fraction profiles after core helium depletion, terminated prior to the first thermal pulse at $\log(L/L_\odot) > 3.0$. Middle: mass fraction profiles at the first `wd_builder` model step. These profiles have been shaved of their excess hydrogen envelope prior to running on the WD cooling track. These are the initial hot WD profiles. Right: mass fraction profiles when the models have cooled to $T_{\rm eff} = 10{,}000$ K. The smoothness in the profiles reflects the element diffusion processes included in the calculation. Bottom: mass fraction profiles with core overshooting (OV) during the CHeB phase, in the same format as above. Green curves represent positive σ_i ^{12}C(α, γ)^{16}O reaction rates, gray curves represent negative σ_i ^{12}C(α, γ)^{16}O reaction rates. For both positive and negative σ_i, the shading grows fainter the further σ is from the standard rate ($\sigma = 0$; black curve).

convection (Jermyn et al. 2023), rotationally induced mixing, semiconvection, thermohaline mixing, or first-order phase separation of the CO mixture (Bauer 2023).

3.2. Evolutionary Differences after the Main Sequence

How do the final WD profiles for the NOV and OV sets in Figure 2 relate to their respective CHeB evolution histories? Figure 3 shows the Kippenhahn diagrams for the $\sigma = 0.0$ models for NOV (left) and OV (right). This figure shows the CHeB phase until the $\log(L/L_\odot) > 3.0$ termination point, spanning $\simeq$0.93–1.10 Gyr. During this period the total mass of our models is $\simeq 2.1\,M_\odot$, but we show only the innermost $\simeq 0.65\,M_\odot$ to capture the evolution history that ultimately defines the CO WDs.

There are immediate differences between the NOV and OV CHeB evolution histories for the $\sigma = 0.0$ models. These differences are similar for any given σ_i models, and a link to an interactive figure is provided in the online journal to see each rate's OV versus NOV comparison in greater detail.

For the NOV set, we see gradual growth of the convective core throughout the CHeB phase; the noted central mass fraction isotopes smoothly deplete/grow to reach their final mass fractions; the convective cores have no apparent splitting during the CHeB phase. Further, there is a pure radiative zone throughout the CHeB history. In comparison, the OV set shows convective cores that ebb and flow in their extent, in a sawtooth-like manner; overshooting extends past the inner convective core in a fairly consistent mass length; the OV central mass fraction isotopes ebb and flow symmetrically with the mixing phenomena at any given time.

We also see splittings of the convective core in the OV set. These splittings were not observed in any of the NOV models

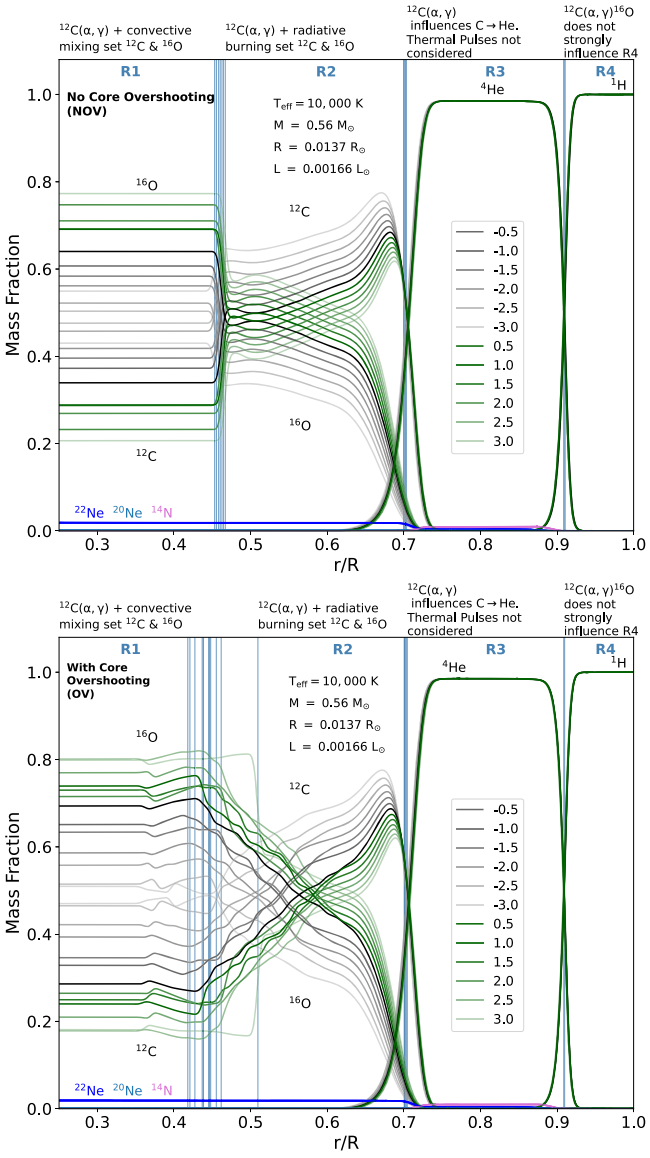

Figure 2. Composition profiles after the NOV (top) and OV (bottom) models cool to $T_{\rm eff} = 10{,}000$ K. Region boundaries are indicated by vertical blue lines, and the σ_i colors are the same as in Figure 1.

during the CHeB phase. We presume they are a result of overshoot inclusion. This introduces "pollution" to the pureness of the radiative burning zone, which becomes the R2 region of the WD. The pollution is seen by observing that some of the split-convection zone surpasses the $\log(L/L_\odot) > 3.0$ R2 inner edge boundary. This boundary becomes the inner edge of R2 in the cool WDs. The amount of convective pollution within the OV set is minor for $\sigma_{0.0}$, but varies with σ_i. Figure 3 qualifies R2 as "Mostly Radiative" for the NOV set due to localized, short-lived, subtle convective occurrences between $\simeq$0.30 and 0.35 $M_\odot$ near core helium depletion energetics. Composition profiles are less sensitive to mixing after CHeB is complete. Any convective pollution from these brief convective periods in the NOV set are insignificant compared to the convective pollution introduced in the OV set.

For both sets, nuclear burning primarily takes place within the convective core. Both sets also show similar burning regions in the mantle outside the core, in the radiative zone. Near the end of core helium depletion, nuclear burning in the core extends past the convective and overshooting core regions in the OV set, and burns into the radiative zone. This is not seen in the NOV set.

3.3. White Dwarf Adiabatic Pulsation Analysis

How do these evolutionary and WD structural differences impact the WD ^{12}C(α, γ)^{16}O reaction rate pulsation signatures? We first stress the importance of the NOV models' R2 pure radiative zone during the CHeB. The trapped-mode σ_i signature found in C22 resonates the most with this region. We want to determine if this signature, or any other σ_i pulsation signature, exists when overshooting is considered at the inner R2 boundary during CHeB. First, we compare the NOV WD pulsation signatures in this work to those in C22.

3.4. NOV Set versus C22

In this section, we briefly describe the main differences between the NOV and C22 models. The models in C22 used a 30-isotope chemical network compared to the 23-isotope network used here; see Appendix B for a comparison. Also, the temporal resolution was greater in C22, especially through CHeB. The most important difference in the NOV models is that we terminated the evolution prior to the first thermal pulse; the models in C22 continued the evolution through the thermal pulse phase of evolution. The overall composition structure of the R1 and R2 regions in our NOV models are quite similar to those in C22.

The NOV set of models in this work found two WD g-mode signals for σ_i rather than one. This is shown in the top two panels of Figure 4. Both panels show snapshots of the percent period differences as a function of σ_i, at $T_{\rm eff} = 11{,}500$ K (bright green) and $T_{\rm eff} = 10{,}000$ K (blue), respectively. The y-axis label defines the period differences as $(P_{\sigma_0} - P_{\sigma_i})/P_{\sigma_0}$. That is, they are normalized to the pulsation periods of the $\sigma = 0$ NOV model. The first panel is the signal from g_2, and the second is the signal from g_6. In C22, the g-mode signature was a trapped mode. Trapped modes are identified from local minima in the kinetic energy diagram (Winget et al. 1981; Brassard et al. 1991). The NOV kinetic energy diagrams for all σ_i at these snapshots are shown in the bottom-left and right panels of Figure 4, following Equation (2) in C22 (Unno et al. 1989; Córsico et al. 2002). The figure caption explains the coloring for σ_i. At $T_{\rm eff} = 11{,}500$ K (bottom-left panel), the first apparent trapped mode occurs at g_6 for all σ_i, with the exception of $\sigma = 0.5$, which has its first local minimum of $E_{\rm kin}$ at g_5. By $T_{\rm eff} = 10{,}000$ K (bottom-right panel), all σ_i have the first local minimum in $E_{\rm kin}$ at g_6, including $\sigma = 0.5$. This is important as g_6 is one of our signature modes for σ_i. These findings are in overall agreement with C22. The trapped g_6 mode signature is not linear with σ_i, but overall shows $\sigma_i < 0$ to have longer periods than $\sigma = 0.0$, and $\sigma_i > 0$ to have shorter periods than $\sigma = 0.0$. The R2 contribution to the g_6 period in our NOV models was $\sim$25%. Other regions equally contributed between $\sim$20% and 30%, meaning that the trapped mode from our NOV set is more equitably trapped among the four regions. Thus, its credibility from R2 is not as strong as in C22. Nonetheless, it is not a negligible contribution and can still serve as a viable probe for σ_i.

Our other g-mode signal, g_2, does not appear to be trapped by definition (see other highlighted mode in bottom of Figure 4). However, the g_2 period differences are directly

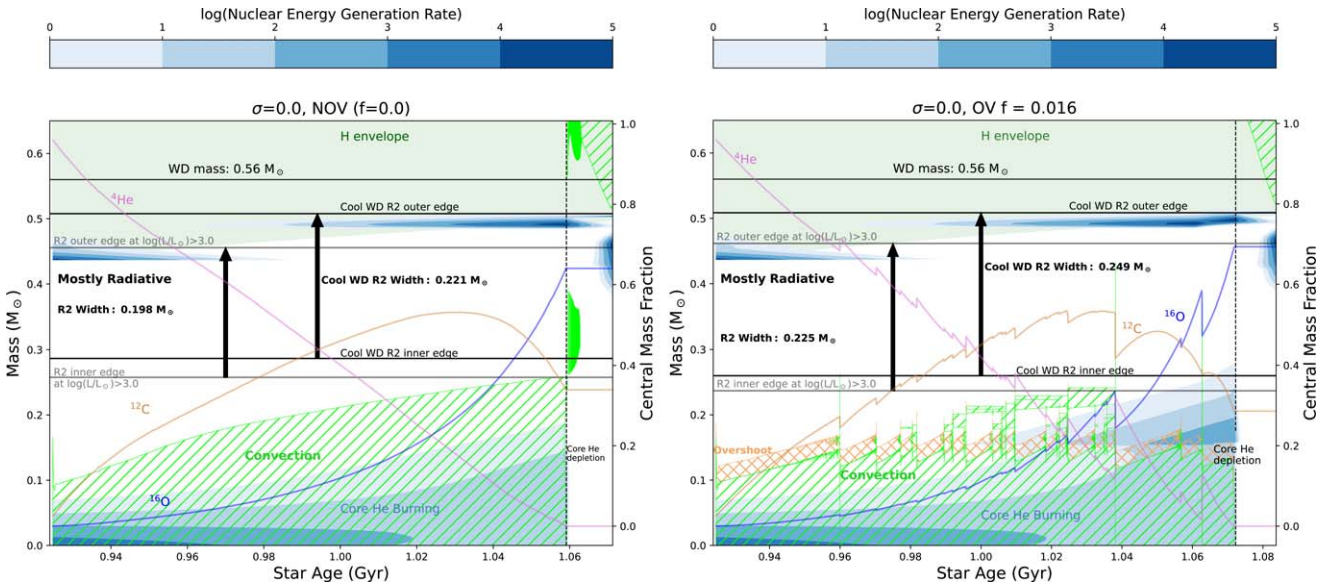

Figure 3. Kippenhahn diagrams for the NOV (left) and OV (right) $\sigma = 0.0$ models. The x-axis is the respective stellar model's age, the left y-axis is the mass coordinate, the right y-axis is the central mass fraction of the isotopes. Bright green areas represent convection, blue shaded regions depict nuclear burning (see color bar), white areas represent radiation, and yellow-gold areas represent overshooting (right figure). The light green area shows the hydrogen envelope. The solid pink curve is the central ^{4}He mass fraction, the solid dark blue curve is the central ^{16}O mass fraction, and the dark yellow curve is the central ^{12}C mass fraction. The dashed line shows core helium depletion. The evolution was terminated when $\log(L/L_\odot) > 3.0$ for all stellar models, and the figures are plotted until that point. Annotated is the radiative R2 region's edges and widths. An interactive figure is provided in the online version. Its functionality compares the NOV and OV Kippenhahn diagrams for any given σ_i ^{12}C(α, γ)^{16}O reaction rate. To use the interactive figure, click on the "sigma" slider at the top, and slide through the indices 0 through 12. Sliding through each index provides the user the side-by-side comparison of the Kippenhahn diagrams for the respective σ_i ^{12}C(α, γ)^{16}O reaction rate used in the evolution. Index 0 starts at $\sigma_{-3.0}$ and index 12 ends at $\sigma_{3.0}$.

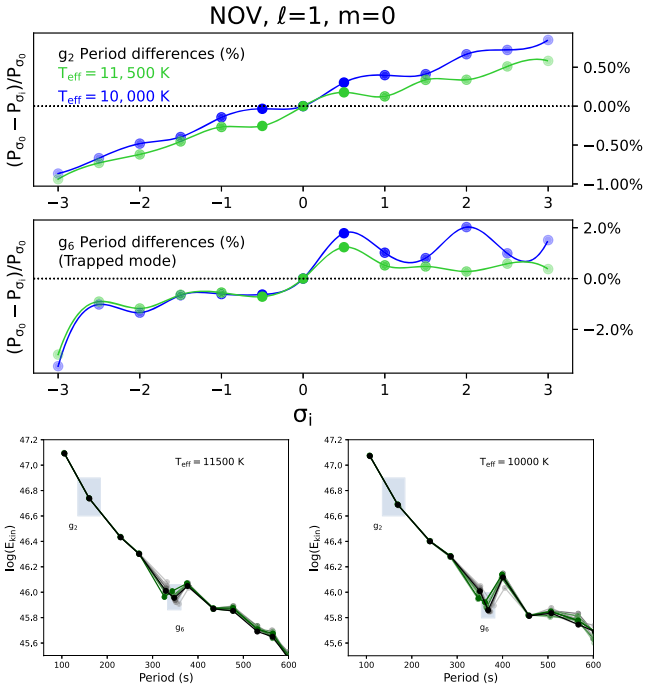

Figure 4. Top two: NOV set's signature adiabatic pulsation modes shown at $T_{\rm eff} = 11{,}500$ K (bright green), and $T_{\rm eff} = 10{,}000$ K (blue), respectively. The first panel shows the signal from the g_2 mode; the second shows the signal from the g_6 trapped mode. Bottom: the kinetic energy diagrams for all σ_i at $T_{\rm eff} = 11{,}500$ K (left) and $T_{\rm eff} = 10{,}000$ K (right), respectively. The green dots/lines represent $E_{\rm kin}$ for $\sigma_i > 0$, gray for $\sigma_i < 0$, black for $\sigma = 0$. The shading of color gets fainter the further away from $\sigma = 0$.

proportional to σ_i (first panel of Figure 4). This suggests that g_2 is likely distinguishing CO features in the inner regions better than other g-modes. The additional g_2 signal was either recovered or contrived as a consequence of excluding the thermal pulse history in the evolution. This was the only procedural difference between our models and those in C22. The direct impact of this procedural difference is expressed by the nearly uniform ^{12}C and ^{4}He profiles after the C $\rightarrow$ He transition (see Figure 1). C22 showed variations in these profiles that stemmed from variations in the thermal pulse histories. Eliminating such chemical variations near the R2–R3 interface can placate the g-modes' sensitivity to the R3 and R4 regions, especially for low-order g-modes such as g_2. Figure 9 in C22 shows g_2 distinguishes σ_i in their thinner-atmosphere sequence of models. Thinner atmospheres may also lessen sensitivities to outer regions, allowing lower-order g-modes like g_2 to probe deeper into the CO interior. We therefore suspect g_2 is a viable probe for σ_i if there are uniform composition profiles at the R2–R3 boundary, and/or thinner WD atmosphere models.

We conclude that our NOV pulsation signature results are overall consistent with C22; we find certain low-order adiabatic WD g-modes that probe the ^{12}C(α, γ)^{16}O reaction rate probability distribution function. With our two signature modes established, we now discuss the impact that overshoot inclusion has on these pulsation signatures.

3.5. Detailed Analysis of Differences

We first show the pulsation periods as a function of surface temperature for all σ_i models in Figure 5. Black dots mark the NOV periods and gray dots mark the OV periods. G-modes with radial orders $n = 1$–10 are annotated, all for $\ell = 1$. Figure 5 shows that there are differences in the periods between the NOV and OV sets, but there is no global systematic offset; the differences between the OV and NOV periods for any given g-mode is random. This is the case even

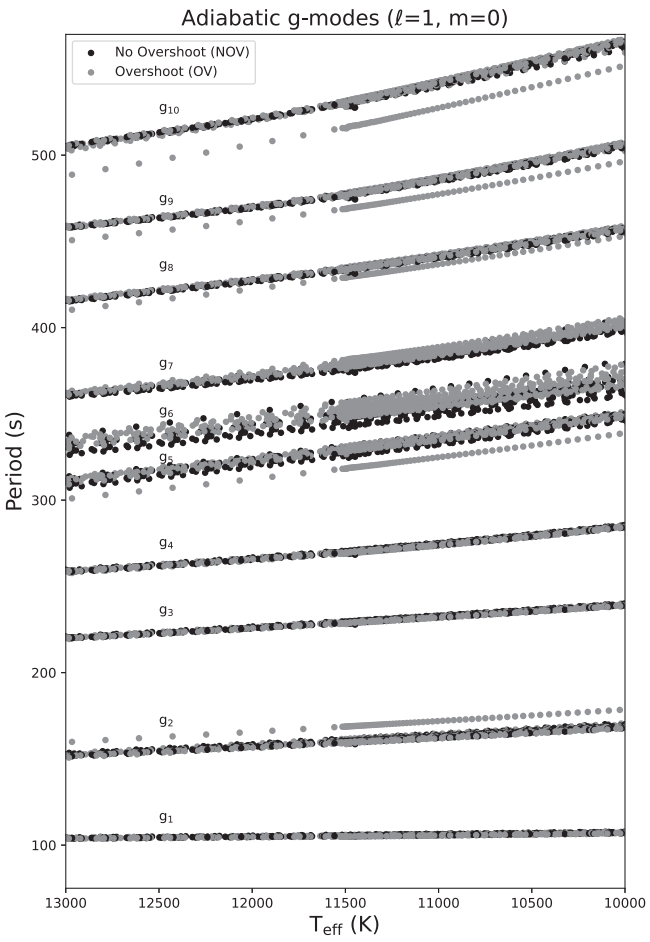

Figure 5. Pulsation periods as function of $T_{\rm eff}$ for the NOV (black) and OV (gray) model sets.

when σ_i is constant. We find that g_6 shows the largest spread in the periods of the models. Further, the kinetic energy diagrams for all models show that g_6 was a trapped mode by $T_{\rm eff}$ = 10,000 K for every model, regardless of the σ_i, NOV/OV prescription. Since g_6 is one of the signals for σ_i in the NOV models, we point out this feature in Figure 5. We will touch on the cause of the larger spread later, but now focus our attention on the detailed pulsation properties of the signature g_2 and g_6 modes.

Figure 6 shows, from top to bottom, the mass fraction profiles, B, and the g_6 and g_2 mode weight functions, ζ, for the final WDs at $T_{\rm eff}$ = 10,000 K. The left and right columns are the NOV and OV results, respectively. Here, we show the comparison for $\sigma = 0.0$, but an interactive figure link is provided in the online article to compare these properties for any σ_i. For all σ_i, NOV/OV comparisons, the dotted vertical lines mark the region boundary locations in each panel. This is useful to compare where the boundary locations are across multiple profile properties. For instance, the R1–R2 boundary marks the C → O transition region, the first most prominent peak in B, and the first peak-like features in $g_6\,\zeta$ and $g_2\,\zeta$ in the NOV case. Comparing the OV column to the NOV column, we see the global impacts from overshooting. Overall, prominent features in the NOV set are lessened in magnitude in the OV set. The C → O transition is more gradual, lessening the composition gradient at the defined boundary. This remarkably impacts the shape of B. The first prominent peak after max(O) is much lower in magnitude for all σ_i, and is not the only outstanding peak near the boundary. There are now multiple, smaller peaks in B and the $g_6\,\zeta$ near the R1–R2 boundary as opposed to one. There are slight deviations between NOV and OV in these profiles for the R3 and R4 regions of the WD, but the R1 → R2 region in these profiles was affected most.

The $g_6\,\zeta$ and $g_2\,\zeta$ panels in Figure 6 note the weight percentages per region in the WD. This tells each region's contribution to the overall mode period (frequency). An interesting result for all σ_i is that both the g_2 and g_6 modes decrease the amount of weight in R1 when overshoot is included, and increase the amount of weight in R2. There is also a slight decrease in the weight of R3 for g_2 for all σ_i when overshoot is included. These results are important. The R2 region is the most reliable region in terms of extracting the σ_i rate signature. When overshoot is included, the R2 contribution to the overall pulsation modes in g_2 and g_6 are accentuated, implying that these modes more reliably distinguish σ_i than the NOV set. A quantitative analysis of each region's weight percentage contribution per σ_i is given for both sets in Tables 1 and 2 for g_2 and g_6, respectively. Overall, Table 1 shows that R2 and R3 are the most heavily weighted regions for g_2's period. G_6 has more equitable weight dispersed across regions, but the combined weight of R1 and R2 accounts for ∼50% of the g_6 period for any given model. As identified in Figures 2 and 6, R1 and R2 are the most impacted regions in this study. A g-mode with about half its weight from those regions may pick up the detailed differences more so than modes weighted more in outer regions. This may explain why Figure 5 shows a larger spread in the g_6 periods as this g-mode is likely picking up the R1 and R2 contributions to its period better than other g-modes.

When an integer multiple, q, of the local radial wavelength, λ_r, for a given g-mode nearly matches the width of a certain region(s) in a star, the g-mode resonates with that region(s). Figure 7 shows $q \cdot \lambda_r(R_\odot)$ as a function of radius $R\,(R_\odot)$ for the g_2 and g_6 modes. The NOV set does not show any particular close matches for any region. However, the closest matches to the R2 width were the λ_r curves of g_2, $q = 1$, and g_6, $q = 2$. Further, the g_2, $q = 2$ and g_6, $q = 3$ modes were best at resonating with R3. Larger q values may show stronger resonance with R4. The resonance with R2 is enhanced in the OV set. The g_2, $q = 1$ and g_6, $q = 2$ λ_r curves match much more closely to the R2 width in the OV set. This implies that overshoot has enhanced the g-mode resonance for our signature modes in the region that was constructed mainly from radiative burning (Figure 3). We also see stronger resonance within the R1 region with the g_2, $q = 1$ λ_r curve.

Will the differences between the NOV and OV sets in Figure 6 impact the WD ^{12}C(α, γ)^{16}O σ_i pulsation signatures shown in Figure 4? Figure 8 shows the resulting relative period percent differences as a function of σ_i at $T_{\rm eff} = 11{,}500$ K (bright green) and $T_{\rm eff} = 10{,}000$ K (blue). The period differences are negative for σ_i with longer periods than the $\sigma = 0$ model, and are positive for σ_i with shorter periods than the $\sigma = 0$ model for the given NOV or OV set. The left of this figure shows the period differences for g_2, and the right shows the period differences for g_6. The NOV set is indicated by the dotted lines and the OV set is the solid lines.

Looking at g_2, the period differences between NOV and OV at $T_{\rm eff} = 11{,}500$ K are minimal: both sets show a trend of decreasing period with increasing σ_i. At $T_{\rm eff} = 10{,}000$ K, the

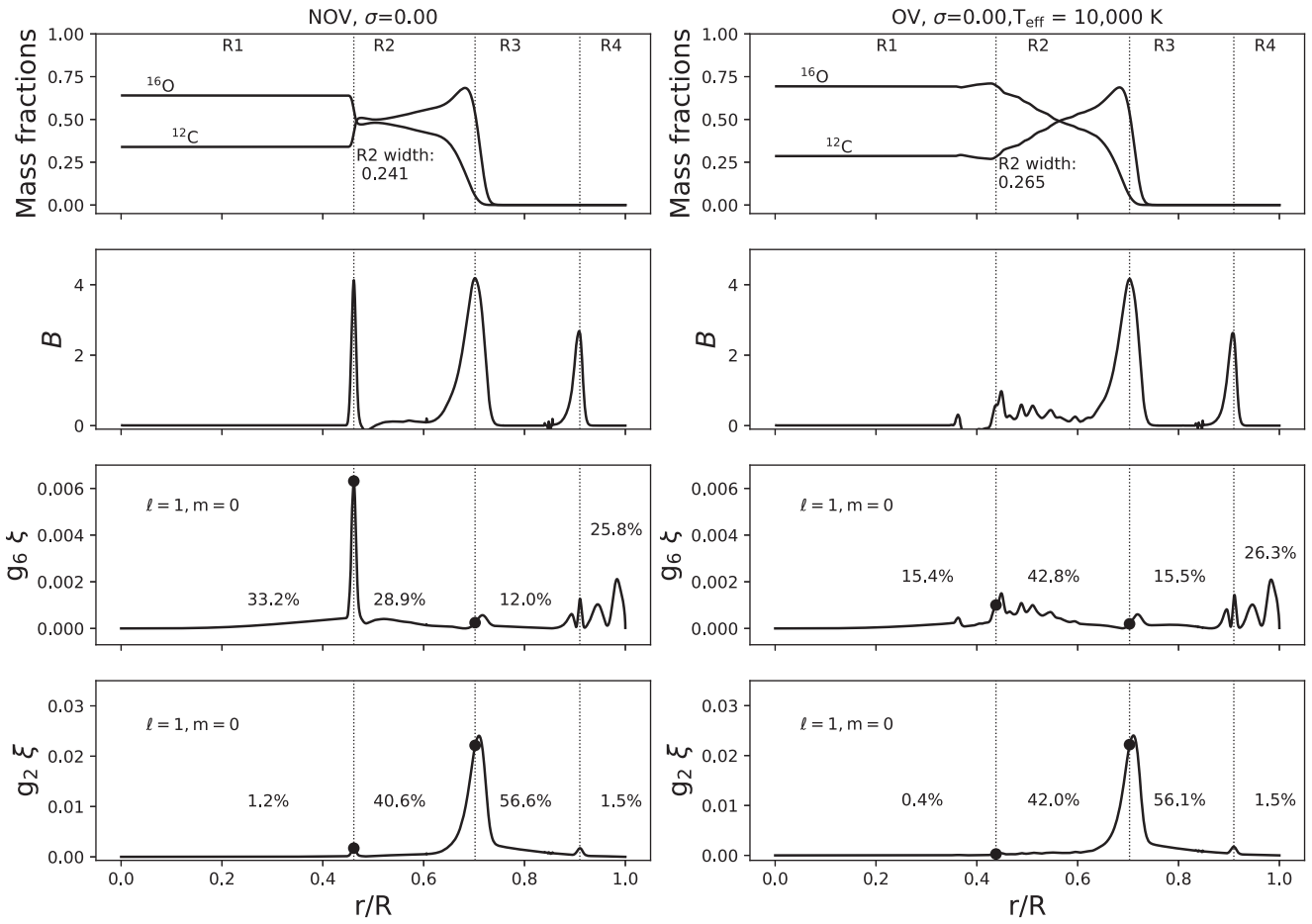

Figure 6. Top to bottom: mass fractions of ^{12}C and ^{16}O; B profile; normalized weight function profile for the g_6 mode; normalized weight function profile for the g_2 mode. The left column shows the NOV results, and the right column shows the OV results. Both figures are for $\sigma = 0.0$, $T_{\rm eff} = 10{,}000$ K. The R1–R4 region boundaries are indicated by dashed vertical lines. An interactive figure is provided in the online version. Its functionality compares the NOV and OV diagrams, as structured in this figure, for any given σ_i ^{12}C(α, γ)^{16}O reaction rate. To use the interactive figure, click on the "sigma" slider at the top, and slide through indices 0 through 12. Sliding through each index provides the user the side-by-side comparison of the diagrams for the respective σ_i ^{12}C(α, γ)^{16}O reaction rate used in the evolution. Index 0 starts at $\sigma_{-3.0}$ and index 12 ends at $\sigma_{3.0}$.

Table 1
g_2 Weight Function Percentages per WD Region

	R1		R2		R3		R4	
σ_i	NOV	OV	NOV	OV	NOV	OV	NOV	OV
−3.0	0.91	0.75	40.6	41.3	57.0	56.4	1.47	1.47
−2.5	1.14	0.99	40.2	44.2	57.2	52.9	1.43	1.94
−2.0	1.05	0.52	40.2	41.1	57.2	56.9	1.54	1.53
−1.5	1.18	0.53	39.5	41.7	57.9	56.2	1.50	1.50
−1.0	1.16	0.27	40.4	41.5	56.9	56.8	1.48	1.46
−0.5	1.15	0.18	38.8	42.1	58.6	56.3	1.43	1.49
0.0	1.25	0.38	40.6	42.0	56.6	56.1	1.52	1.47
0.5	1.44	0.49	40.8	41.9	56.2	56.2	1.52	1.47
1.0	1.28	0.31	40.4	41.4	56.9	56.7	1.49	1.58
1.5	1.32	0.28	39.9	41.4	57.2	56.8	1.50	1.51
2.0	1.35	0.19	39.4	40.8	57.8	57.5	1.50	1.49
2.5	1.25	0.42	38.3	41.6	58.9	56.6	1.47	1.45
3.0	1.39	2.06	40.2	39.6	56.9	56.8	1.59	1.52

Table 2
g_6 Weight Function Percentages per WD Region

	R1		R2		R3		R4	
σ_i	NOV	OV	NOV	OV	NOV	OV	NOV	OV
−3.0	25.5	20.1	25.6	32.4	21.1	19.8	27.8	27.8
−2.5	33.1	19.1	29.5	33.5	13.1	20.2	24.2	24.2
−2.0	32.3	16.6	30.8	36.3	13.9	19.7	23.0	23.0
−1.5	33.5	17.3	29.6	39.1	12.6	17.3	24.4	24.4
−1.0	33.8	13.4	30.0	43.1	12.9	17.4	23.3	23.3
−0.5	33.5	11.7	29.8	47.5	12.8	14.9	23.9	23.9
0.0	33.2	15.4	28.9	42.8	12.0	15.5	25.9	25.9
0.5	26.6	16.4	22.5	41.0	13.8	14.0	37.1	37.1
1.0	31.2	14.1	27.1	43.8	12.4	16.1	29.3	29.3
1.5	32.2	13.7	27.4	46.7	12.2	14.7	28.3	28.3
2.0	25.5	11.7	23.0	48.1	14.1	14.3	37.3	37.3
2.5	30.9	14.2	28.0	42.5	12.5	13.8	28.6	28.6
3.0	30.1	32.0	25.5	26.2	12.4	13.8	32.0	32.0

OV set shows an overall decrease in the percent differences, and a slightly greater variation in the overall σ_i versus g_2 period difference shape. However, at both temperatures the same pattern of the g_2 period decreasing with increasing σ_i is sustained with overshoot inclusion. Further, the magnitudes of percent differences, ranging from $\simeq -1.5$ to $+1.0$, are within the detectable threshold (Chidester et al. 2021).

The OV set shows greater deviation from the NOV line of period percent differences in g_6 more so than g_2. This is most likely because g_6 is more sensitive to changes from R1 than g_2.

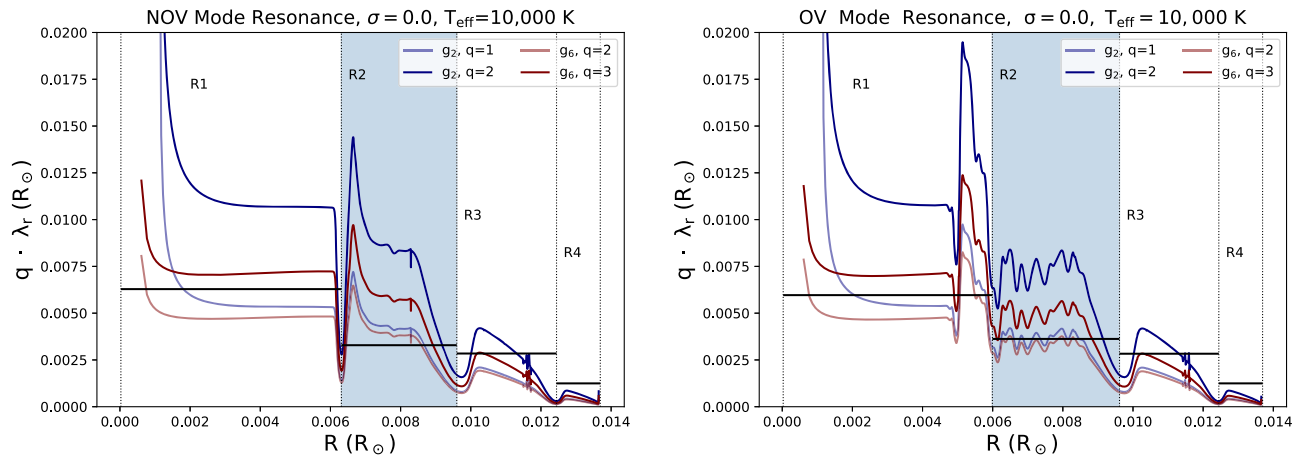

Figure 7. Integer multiples of the local radial wavelengths $q \cdot \lambda_r$ for g_2 and g_6 as a function of the star's radius R. Mode resonance occurs when $q \cdot \lambda_r$ closely matches the width of a certain region(s) in the star. The left panel is the NOV set's mode resonance and the right panel is the OV set's mode resonance. In both panels, the black horizontal lines mark the respective region widths. Blue curves show $q \cdot \lambda_r$ for g_2, and maroon curves show $q \cdot \lambda_r$ for g_6. The q values are stated in the legend.

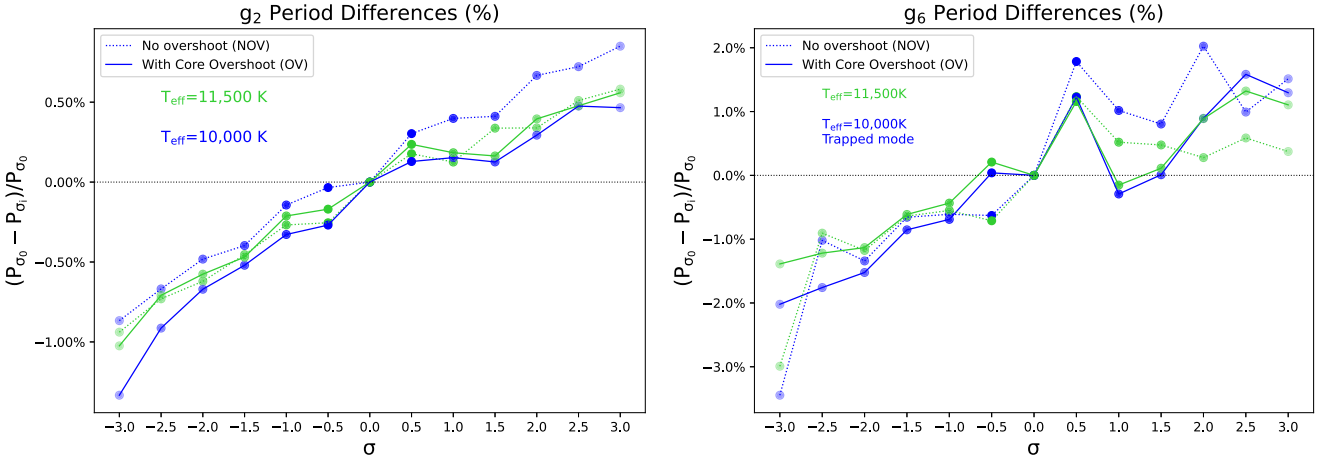

Figure 8. Adiabatic g_2 (left) and g_6 (right) mode signatures for the NOV and OV sets, at $T_{\rm eff} = 11{,}500$ K (bright green) and $T_{\rm eff} = 10{,}000$ K (blue), respectively.

Nonetheless, despite the $\sigma_{=-0.5}$ and $\sigma_{+1.0}$ outliers, the overall trend remains: $\sigma_i < 0$ generally have longer periods than σ_0, and $\sigma_i > 0$ generally have shorter periods than σ_0. Once again, the magnitudes of the relative period percent differences surpass the observable threshold.

An interesting note is that for both g_2 and g_6 signals, the percent differences change more in the NOV set, as the models cool from $T_{\rm eff} = 11{,}500$ to $T_{\rm eff} = 10{,}000$ K, than the OV set. The OV set showed nearly the same period differences at both temperatures.

4. Discussion

C22 found pulsation signature(s) for the experimental ^{12}C(α, γ)^{16}O reaction rate probability distribution function. They describe four sensitivities that may impact this result: the width of the O → C transition, mixing during CHeB, the thermal pulse history on the AGB, and the 3α reaction rate. This work investigates the impact that overshoot inclusion had on the ^{12}C(α, γ)^{16}O reaction rate pulsation signature(s). In doing so, we address the width of the O → C transition and mixing during CHeB. Further, by ignoring the thermal pulse history in our models, we also address the sensitivity to the number of thermal pulses, albeit the trivial case when the number of thermal pulses is zero. In the following paragraphs, we discuss how these three sensitivities impacted our results. We further caution how our results could be impacted from further sensitivity investigations.

Including overshooting overall increased the width of the O → C transition for all σ_i cool WDs. This lessened the sharp peak in B at the O → C transition, and decreased the peak in $g_6\,\zeta$ at the O → C transition. While the transition peak was lessened and dispersed into R2, widening the O → C transition showed an enhancement of both the weight contribution to the R2 region for g_2 and g_6, and the R2 resonance with λ_r for g_2 and g_6. The widening of the O → C transition was from the combined effects of overshoot inclusion and the σ_i prescription. We conclude that widening the O → C transition imposes differences in B, ζ, and the pulsation periods. Despite these changes, we still find the g_2 and g_6 relative period differences in the NOV and OV sets to distinguish the ^{12}C(α, γ)^{16}O reaction rate probability distribution function. Namely, the pattern of decreasing period with increasing σ_i persisted in both NOV and OV sets. By itself, the inclusion of overshooting does not destroy the seismic signatures of the ^{12}C(α, γ)^{16}O reaction rate in our WD models—which was the primary question of this study.

We caution that increasing (decreasing) the width of the O → C transition in CO WD models could potentially yield different results. Our CO WD models were informed from their evolution history, with the stated model parameters. Thus, an increase (decrease) of the width of the O → C transition may come from choosing different mixing processes, prescriptions and parameters, such as for convection and overshooting. A change in the width of the O → C transition may also come from mixing processes not considered in this study such as time-dependent convection (Jermyn et al. 2023), rotationally induced mixing, semiconvection, thermohaline mixing, or first-order phase separations of the CO mixture (Bauer 2023).

Ignoring the thermal pulse history gave an additional low-order adiabatic g-mode signature for σ_i, namely the g_2 signal. This signal was not found in C22, where the thermal pulse history was included. Future studies on the thermal pulse phase of evolution with different temporal and spatial resolutions are needed to determine the sustainability of the g_2 signal as a probe for σ_i. Concurrently, future studies could also explore the interaction, if any, between the thermal pulses and overshooting during CHeB on the chemical profiles.

The CO cores of WDs are the result of the competition between 3α and $^{12}C(\alpha, \gamma)^{16}O$ during CHeB. An experimental 3α reaction rate probability distribution function, similar to the existing one for $^{12}C(\alpha, \gamma)^{16}O$ (deBoer et al. 2017; Farag et al. 2022; Mehta et al. 2022, C22), does not yet exist to our knowledge, although a probability distribution function could be constructed using the STARLIB reaction rate library (Sallaska et al. 2013; Fields et al. 2016, 2018). Future studies involving both reaction rate probability distribution functions could probe properties of DAV WD models in the 3α rate–$^{12}C(\alpha, \gamma)^{16}O$ rate plane. For example, the 3α reaction rate is likely to slowly modulate the central ^{16}O mass fraction at any $^{12}C(\alpha, \gamma)^{16}O$ reaction rate because 3α controls the production of ^{12}C. The $^{12}C(\alpha, \gamma)^{16}O$ reaction rate will likely modulate the central ^{16}O mass fraction more strongly at any 3α reaction rate. We speculate that the radiative region R2 will exist in all such models. We also suspect that all such models, whether terminated at the first thermal pulse or evolved through the thermal pulse phase, will show a trapped mode, with substantial trapping from R2, that best probes the $^{12}C(\alpha, \gamma)^{16}O$ burning reaction rates (i.e., g_6 in this work; and see Figure 9 in C22). We caution that the relative period shifts we find in this work from considering the $^{12}C(\alpha, \gamma)^{16}O$ probability distribution and overshooting may change when a 3α reaction rate probability distribution function is also considered.

De Gerónimo et al. (2017) found that including overshooting impacted ensuing WD pulsations by ∼2–5 s. Their results were independent of their $^{12}C(\alpha, \gamma)^{16}O$ reaction rate uncertainty evaluation. We combined the effects of overshooting and the $^{12}C(\alpha, \gamma)^{16}O$ reaction rate sensitivities in our pulsation analysis, and likewise find period differences of similar magnitudes. Our $^{12}C(\alpha, \gamma)^{16}O$ reaction rate analysis spanned the current experimental probability distribution function, which analyzed different rate values than those explored in De Gerónimo et al. (2017). They concluded that the $^{12}C(\alpha, \gamma)^{16}O$ uncertainty was less relevant than overshooting. In this study, we find that the combined effects from overshooting and the $^{12}C(\alpha, \gamma)^{16}O$ reaction rate probability distribution function yields remarkable differences in the structure of the CO WDs, and pulsation differences. Despite these differences, we still find pulsation signatures for σ_i.

5. Summary

We conducted a search for signatures of the current experimental $^{12}C(\alpha, \gamma)^{16}O$ reaction rate probability distribution function in the pulsation periods of CO WD models with the inclusion of overshooting. We found two signature adiabatic g-modes that show period differences with the reaction rate probability distribution function σ_i trend regardless of whether or not overshoot is included. We find a g_2 period difference signature is inversely proportional to σ_i. Without overshoot, the g_2 relative period differences span $\pm 0.9\%$. With overshoot, the g_2 relative period differences range from -1.33% to 0.47%. The average magnitude of the relative period differences for g_2 were 0.46% and 0.44%, respectively. The g_6 period differences were larger in magnitude, spanning from -3.44% to 1.78% for NOV and -2.02% to 1.58% for OV. The average magnitude of the g_6 period differences were 1.21% and 0.95%, respectively. The average magnitudes of the g_2 and g_6 period differences were slightly decreased from the NOV set.

We found that the R2 weight contribution to these g-modes was enhanced with overshoot inclusion. The R2 region remains the best identifying region for tracing the $^{12}C(\alpha, \gamma)^{16}O$ reaction rate probability distribution function. This is because, even with overshoot inclusion, it is predominantly constructed by radiative burning during CHeB. Regardless of whether or not overshooting is considered, we find the following:

1. Two signature g-modes, g_2 and g_6, probe σ_i.
2. g_2 is inversely proportional to σ_i, and g_6 is a trapped mode.
3. The g_2 and g_6 periods are generally shorter for positive σ_i and longer for negative σ_i.
4. Both signatures have period deviations within the detectable regime.

These findings suggest that an astrophysical constraint on the $^{12}C(\alpha, \gamma)^{16}O$ reaction rate probability distribution function remains, in principle, extractable from the period spectrum of observed variable WDs.

Acknowledgments

We thank James Deboer for sharing the $^{12}C(\alpha, \gamma)^{16}O$ probability distribution function, Josiah Schwab for sharing `wd_builder`, and Pablo Marchant for sharing `mkipp`. We acknowledge using ChatGPT (OpenAI 2023) to polish the language of one paragraph (Vishniac 2023). This research is supported by NASA under the Astrophysics Theory Program grant No. NNH21ZDA001N-ATP, and in part by the National Science Foundation under grant No. NSF PHY-1748958. This research made extensive use of the SAO/NASA Astrophysics Data System (ADS).

Software: `MESA` (Paxton et al. 2011, 2013, 2015, 2018, 2019; Jermyn et al. 2023, https://docs.mesastar.org/), `MESASDK` 20190830 (Townsend 2019a, 2019b), `wd_builder` https://github.com/jschwab/wd_builder, `GYRE` (Townsend & Teitler 2013; Townsend et al. 2018, https://github.com/rhdtownsend/gyre), `mkipp` https://github.com/orlox/mkipp, `matplotlib` (Hunter 2007), `NumPy` (van der Walt et al. 2011), and `ChatGPT` (OpenAI 2023).

Appendix A
Microphysics in MESA

The MESA equation of state (EOS) is a blend of the OPAL (Rogers & Nayfonov 2002), SCVH (Saumon et al. 1995), FreeEOS (Irwin 2004), HELM (Timmes & Swesty 2000), PC (Potekhin & Chabrier 2010), and Skye (Jermyn et al. 2022) EOSs.

Radiative opacities are primarily from OPAL (Iglesias & Rogers 1993, 1996), with low-temperature data from Ferguson et al. (2005) and the high-temperature, Compton-scattering-dominated regime by Poutanen (2017). Electron conduction opacities are from Cassisi et al. (2007) and Blouin et al. (2020).

Nuclear reaction rates are from JINA REACLIB (Cyburt et al. 2010), NACRE (Angulo et al. 1999), and additional tabulated weak reaction rates (Fuller et al. 1985; Oda et al. 1994; Langanke & Martínez-Pinedo 2000). Screening is included via the prescription of Chugunov et al. (2007). Thermal neutrino loss rates are from Itoh et al. (1996).

Appendix B
Model Optimization and Resolution

B.1. Reduced Chemical Network

The nature of our evolutionary models is computationally expensive. This paper is concerned about overshooting and the $^{12}C(\alpha, \gamma)^{16}O$ reaction rate probability distribution function, which primarily dictate the evolutionary processes and consequences of the CHeB phase. The isotopes most impacted during CHeB are ^{12}C, ^{16}O, and ^{4}He. ^{14}N and ^{20}Ne are the next two most impacted isotopes during CHeB. We thus optimize the efficiency of our models by reducing the chemical network number of isotopes from 30 to 23. The eliminated isotopes are ^{21}Ne, $^{21,22,23}Na$, $^{23,24}Mg$, and ^{56}Fe. A comparison of the resulting inner mass fraction profiles for the five most abundant isotopes for both networks is shown in Figure 9 for each chemical network. This figure shows the profiles at the completion of CHeB. Both network models used the same temporal and spatial resolution during CHeB. The runtime was reduced from a few days to a a few hours on 12 cores. All resolution studies were conducted with $\sigma = 0.0$ without overshoot (NOV).

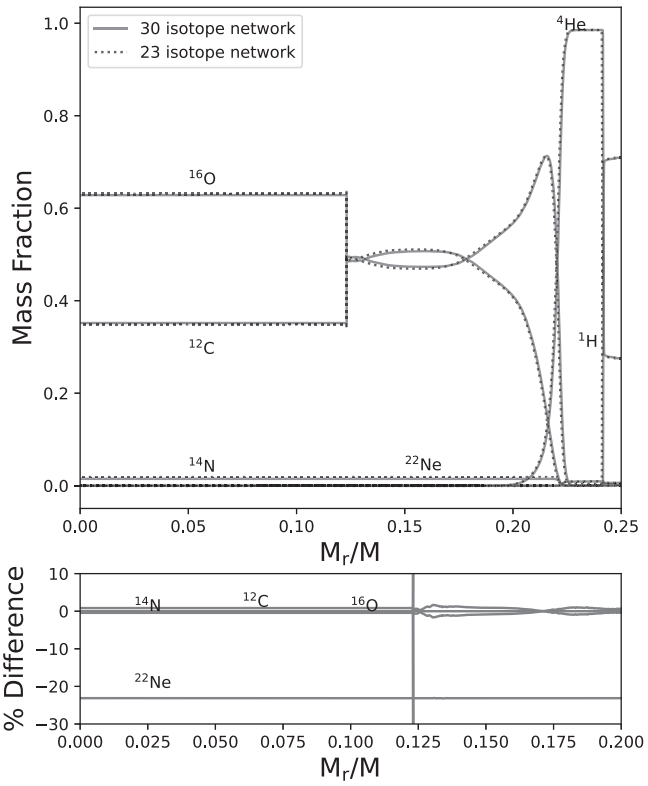

Figure 9. Mass fraction profiles at the completion of CHeB for a 30-isotope (solid) and 23-isotope nuclear reaction network (dotted). Shown are the five most abundant isotopes for both networks.

Reducing the network impacted ^{22}Ne most, with an offset of $\sim$22% more ^{22}Ne in the 23-isotope network. We note that C22 used a 30-isotope network and our overall signature results are persistent through variations in the number of heavier isotopes in the reaction network.

B.2. Temporal Resolution

Several time-step limiters in `MESA` help optimize convergence studies. In this paper, we want to limit the time step to achieve the temporal resolution that yields a smooth evolution of the central ^{4}He, ^{16}O, and ^{12}C abundances during CHeB. We first utilize the `delta_XC_cntr_limit` limiter. This limits the amount the central ^{12}C abundance can change in a given time step. To help optimize computational runtime, we begin limiting the change in central ^{12}C during CHeB for which the central helium abundance $X(^{4}He_c) < 0.6$. This is done by adding the following lines of code in the `MESA run_star_extras.f90` file:

```
if ((s% center_h1<1d-6).and.(s% center_he4 < 0.6).and.(s% delta_XC_cntr_limit>0.001))then
s% delta_XC_cntr_limit=0.0005d0
end if
```

This temporal resolution was used for the 30- and 23-isotope network models. We refer to it as resolution A. The remaining temporal resolution studies were performed using the 23-isotope chemical network.

The next iteration of increased temporal resolution modified the `run_star_extras.f90` file to include the following:

```
if ((s% center_h1<1d-6).and.(s% center_he4 < 0.5).and.(s% delta_XC_cntr_limit>0.001))then
s% delta_XC_cntr_limit=0.0005d0
s% delta_lgT_cntr_limit=5d-4
s% delta_lgT_cntr_hard_limit=1d-3
s% delta_lgRho_cntr_limit=1d-3
s% delta_lgRho_cntr_hard_limit=5d-3
end if
```

This resolution is employed slightly earlier during CHeB, when $X(^{4}He_c) < 0.5$. We added limits to the change in central temperature and density from resolution A. This is known as resolution B.

Our third resolution iteration used the following limiter controls in the `run_star_extras.f90` file:

```
if ((s% center_h1<1d-6).and.(s% center_he4 < 0.999).and.(s% delta_XC_cntr_limit>0.001))then
s% delta_XC_cntr_limit=0.00025
```

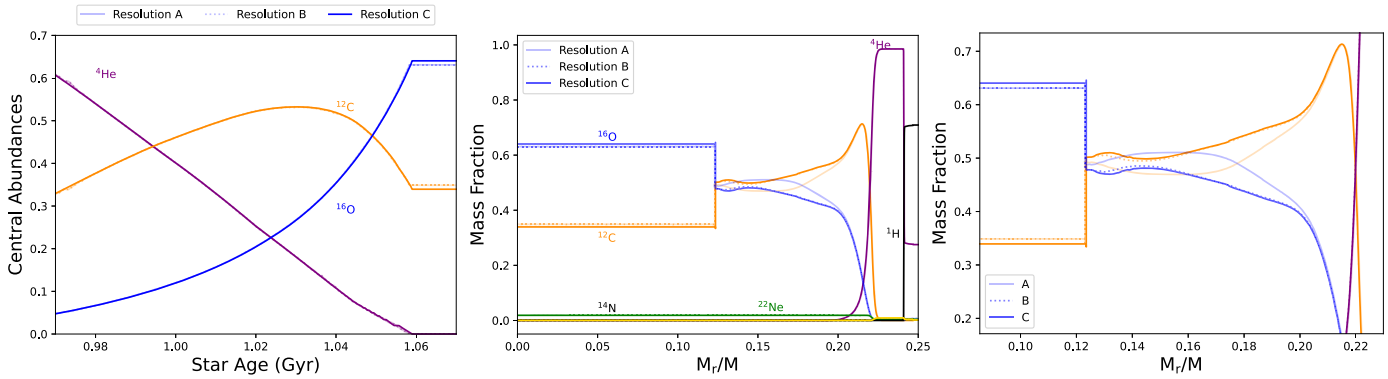

Figure 10. Left: evolution of central mass fractions during CHeB until $\log(L/L_\odot) = 3.0$ at three resolutions. Middle: mass fraction profiles at $\log(L/L_\odot) = 3.0$ for the three resolutions. Right: middle figure zoom in to show differences.

```
s% delta_XO_cntr_limit=0.00025
s% delta_lgT_cntr_limit=2.5d-4
s% delta_lgT_cntr_hard_limit=0.5d-3
s% delta_lgRho_cntr_limit=0.5d-3
s% delta_lgRho_cntr_hard_limit=2.5d-3
end if
```

This is termed resolution C. We have set the limiters at the start of CHeB, and have decreased the limiter values from those in resolution B.

A comparison of resolutions A, B, and C is shown in Figure 10. In each column, the solid light curves represent resolution A, the dotted curves B, and the dark solid curves C.

The left figure shows the evolution of the central abundances of ^{4}He, ^{12}C, and ^{16}O during CHeB, starting when $X(^4\mathrm{He}_c) \lesssim 0.6$ until the completion of CHeB. The central abundances for resolutions A and B are nearly identical. Resolution C varies slightly, with the final central ^{16}O abundance reaching a slightly larger amount than resolutions A and B. Further, all three resolutions show a smooth evolution of these central abundances throughout CHeB.

The middle plot in Figure 10 shows the mass fraction profiles at the completion of CHeB. We show the five most abundant isotope profiles for each resolution. The ^{12}C and ^{16}O profiles for A are noticeably different than the profiles for B and C, especially after the O → C transition. This is more apparent in the right plot of Figure 10, which zooms in on the ^{16}O and ^{12}C profiles of the three resolutions. Resolution B follows A in the core, but then more closely aligns with C after the O → C transition. Since resolutions B and C agree well, with only a slight difference in the central ^{12}C and ^{16}O abundance, we set resolution C as the standard temporal resolution for our 13 models.

ORCID iDs

Morgan T. Chidester https://orcid.org/0000-0002-5107-8639
F. X. Timmes https://orcid.org/0000-0002-0474-159X
Ebraheem Farag https://orcid.org/0000-0002-5794-4286

References

Althaus, L. G., & Córsico, A. H. 2022, A&A, 663, A167
Anders, E. H., Jermyn, A. S., Lecoanet, D., et al. 2022, RNAAS, 6, 41
Angulo, C., Arnould, M., Rayet, M., et al. 1999, NuPhA, 656, 3
Asplund, M., Grevesse, N., Sauval, A. J., & Scott, P. 2009, ARA&A, 47, 481
Bauer, E. B. 2023, ApJ, 950, 115
Blondin, S., Bravo, E., Timmes, F. X., Dessart, L., & Hillier, D. J. 2022, A&A, 660, A96
Blouin, S., Mao, H., Herwig, F., et al. 2023, MNRAS, 522, 1706
Blouin, S., Shaffer, N. R., Saumon, D., & Starrett, C. E. 2020, ApJ, 899, 46
Brassard, P., Fontaine, G., Wesemael, F., Kawaler, S. D., & Tassoul, M. 1991, ApJ, 367, 601
Bravo, E., Domínguez, I., Badenes, C., Piersanti, L., & Straniero, O. 2010, ApJL, 711, L66
Camisassa, M. E., Althaus, L. G., Córsico, A. H., et al. 2016, ApJ, 823, 158
Caputo, F., Castellani, V., Chieffi, A., Pulone, L., & Tornambe, A. J. 1989, ApJ, 340, 241
Cassisi, S., Potekhin, A. Y., Pietrinferni, A., Catelan, M., & Salaris, M. 2007, ApJ, 661, 1094
Cassisi, S., Salaris, M., & Irwin, A. W. 2003, ApJ, 588, 862
Chidester, M. T., Farag, E., & Timmes, F. X. 2022, ApJ, 935, 21
Chidester, M. T., Timmes, F. X., Schwab, J., et al. 2021, ApJ, 910, 24
Chugunov, A. I., Dewitt, H. E., & Yakovlev, D. G. 2007, PhRvD, 76, 025028
Collins, C. E., Gronow, S., Sim, S. A., & Röpke, F. K. 2022, MNRAS, 517, 5289
Constantino, T., Campbell, S. W., & Lattanzio, J. C. 2017, MNRAS, 472, 4900
Cook, K. J., Chevis, A., Eriksen, T. K., et al. 2021, PhRvC, 104, 024620
Córsico, A. H., Althaus, L. G., Benvenuto, O. G., & Serenelli, A. M. 2002, A&A, 387, 531
Córsico, A. H., Althaus, L. G., Miller Bertolami, M. M., & Kepler, S. O. 2019, A&ARv, 27, 7
Córsico, A. H., Uzundag, M., Kepler, S. O., et al. 2022, A&A, 659, A30
Cyburt, R. H., Amthor, A. M., Ferguson, R., et al. 2010, ApJS, 189, 240
De Gerónimo, F. C., Althaus, L. G., Córsico, A. H., Romero, A. D., & Kepler, S. O. 2017, A&A, 599, A21
De Gerónimo, F. C., Battich, T., Miller Bertolami, M. M., Althaus, L. G., & Córsico, A. H. 2019, A&A, 630, A100
deBoer, R. J., Görres, J., Wiescher, M., et al. 2017, RvMP, 89, 035007
Eriksen, T. K., Kibédi, T., Reed, M. W., et al. 2020, PhRvC, 102, 024320
Farag, E., Renzo, M., Farmer, R., Chidester, M. T., & Timmes, F. X. 2022, ApJ, 937, 112
Farmer, R., Fields, C. E., Petermann, I., et al. 2016, ApJS, 227, 22
Farmer, R., Renzo, M., de Mink, S. E., Fishbach, M., & Justham, S. 2020, ApJL, 902, L36
Farmer, R., Renzo, M., de Mink, S. E., Marchant, P., & Justham, S. 2019, ApJ, 887, 53
Ferguson, J. W., Alexander, D. R., Allard, F., et al. 2005, ApJ, 623, 585
Fields, C. E., Farmer, R., Petermann, I., Iliadis, C., & Timmes, F. X. 2016, ApJ, 823, 46
Fields, C. E., Timmes, F. X., Farmer, R., et al. 2018, ApJS, 234, 19
Fontaine, G., & Brassard, P. 2002, ApJL, 581, L33
Fowler, W. A., & Hoyle, F. 1964, ApJS, 9, 201
Fryer, C. L., & Kalogera, V. 2001, ApJ, 554, 548
Fuller, G. M., Fowler, W. A., & Newman, M. J. 1985, ApJ, 293, 1
Gautschy, A. 2023, arXiv:2303.11374
Giammichele, N., Charpinet, S., & Brassard, P. 2022, FrASS, 9, 879045
Giammichele, N., Charpinet, S., Brassard, P., & Fontaine, G. 2017, A&A, 598, A109
Giammichele, N., Charpinet, S., Fontaine, G., et al. 2018, Natur, 554, 73
Guichandut, S., & Cumming, A. 2023, arXiv:2301.08769
Hansen, C. J., Kawaler, S. D., & Trimble, V. 2004, Stellar Interiors: Physical Principles, Structure, and Evolution (New York: Springer)
Herwig, F. 2000, A&A, 360, 952

Howell, D. A., Sullivan, M., Brown, E. F., et al. 2009, ApJ, 691, 661
Hoyle, F. 1954, ApJS, 1, 121
Hunter, J. D. 2007, CSE, 9, 90
Iglesias, C. A., & Rogers, F. J. 1993, ApJ, 412, 752
Iglesias, C. A., & Rogers, F. J. 1996, ApJ, 464, 943
Irwin, A. 2004, The FreeEOS Code for Calculating the Equation of State for Stellar Interiors I: An Improved EFF-Style Approximation for the Fermi-Dirac Integrals, https://freeeos.sourceforge.net/eff_fit.pdf
Iserles, A. 1996, A First Course in the Numerical Analysis of Differential Equations (Cambridge: Cambridge Univ. Press)
Itoh, N., Hayashi, H., Nishikawa, A., & Kohyama, Y. 1996, ApJS, 102, 411
Jermyn, A. S., Anders, E. H., Lecoanet, D., & Cantiello, M. 2022, ApJ, 929, 182
Jermyn, A. S., Bauer, E. B., Schwab, J., et al. 2023, ApJS, 265, 15
Kibédi, T., Alshahrani, B., Stuchbery, A. E., et al. 2020, PhRvL, 125, 182701
Korre, L., Garaud, P., & Brummell, N. H. 2019, MNRAS, 484, 1220
Langanke, K., & Martínez-Pinedo, G. 2000, NuPhA, 673, 481
Marchant, P., & Moriya, T. J. 2020, A&A, 640, L18
Mehta, A. K., Buonanno, A., Gair, J., et al. 2022, ApJ, 924, 39
Meng, X.-C., Zhang, J.-J., Zhao, X., Li, L.-P., & Wang, X.-F. 2023, ApJ, 943, 159
Metcalfe, T. S. 2003, ApJL, 587, L43
Metcalfe, T. S., Salaris, M., & Winget, D. E. 2002, ApJ, 573, 803
Metcalfe, T. S., Winget, D. E., & Charbonneau, P. 2001, ApJ, 557, 1021
Miller Bertolami, M. M., Battich, T., Córsico, A. H., Althaus, L. G., & Wachlin, F. C. 2022, MNRAS Lett., 511, L60
Oda, T., Hino, M., Muto, K., Takahara, M., & Sato, K. 1994, ADNDT, 56, 231
OpenAI 2023, arXiv:2303.08774
Paxton, B., Bildsten, L., Dotter, A., et al. 2011, ApJS, 192, 3
Paxton, B., Cantiello, M., Arras, P., et al. 2013, ApJS, 208, 4
Paxton, B., Marchant, P., Schwab, J., et al. 2015, ApJS, 220, 15
Paxton, B., Schwab, J., Bauer, E. B., et al. 2018, ApJS, 234, 34
Paxton, B., Smolec, R., Schwab, J., et al. 2019, ApJS, 243, 10
Pedersen, M. G., Aerts, C., Pápics, P. I., et al. 2021, NatAs, 5, 715
Pepper, B. T., Istrate, A. G., Romero, A. D., & Kepler, S. O. 2022, MNRAS, 513, 1499
Potekhin, A. Y., & Chabrier, G. 2010, CoPP, 50, 82
Poutanen, J. 2017, ApJ, 835, 119
Renzo, M., Farmer, R., Justham, S., et al. 2020, A&A, 640, A56
Rogers, F. J., & Nayfonov, A. 2002, ApJ, 576, 1064
Romero, A. D., da Rosa, G. O., Kepler, S. O., et al. 2023, MNRAS, 518, 1448
Sajadian, S., & Sahu, K. C. 2023, AJ, 165, 96
Salaris, M., & Cassisi, S. 2017, RSOS, 4, 170192
Sallaska, A. L., Iliadis, C., Champange, A. E., et al. 2013, ApJS, 207, 18
Saumon, D., Chabrier, G., & van Horn, H. M. 1995, ApJS, 99, 713
Schatz, H., Becerril Reyes, A. D., Best, A., et al. 2022, JPhG, 49, 110502
Shen, K. J., Kasen, D., Miles, B. J., & Townsley, D. M. 2018, ApJ, 854, 52
Shen, Y., Guo, B., deBoer, R. J., et al. 2023, ApJ, 945, 41
Straniero, O., Domínguez, I., Imbriani, G., & Piersanti, L. 2003, ApJ, 583, 878
Sukhbold, T., Woosley, S. E., & Heger, A. 2018, ApJ, 860, 93
Timmes, F. X., Brown, E. F., & Truran, J. W. 2003, ApJL, 590, L83
Timmes, F. X., & Swesty, F. D. 2000, ApJS, 126, 501
Townsend, R. H. D. 2019a, MESA SDK for Linux v20190503, Zenodo, doi:10.5281/zenodo.2669541
Townsend, R. H. D. 2019b, MESA SDK for Mac OS v20190503, Zenodo, doi:10.5281/zenodo.2669543
Townsend, R. H. D., Goldstein, J., & Zweibel, E. G. 2018, MNRAS, 475, 879
Townsend, R. H. D., & Teitler, S. A. 2013, MNRAS, 435, 3406
Unno, W., Osaki, Y., Ando, H., Saio, H., & Shibahashi, H. 1989, Nonradial Oscillations of Stars (Tokyo: Univ. Tokyo Press)
van der Walt, S., Colbert, S. C., & Varoquaux, G. 2011, CSE, 13, 22
Vishniac, E. T. 2023, BAAS, 55, 016
Weinberg, N. N., Bildsten, L., & Schatz, H. 2006, ApJ, 639, 1018
Werner, K., Reindl, N., Geier, S., & Pritzkuleit, M. 2022, MNRAS Lett., 511, L66
Winget, D. E., van Horn, H. M., & Hansen, C. J. 1981, ApJL, 245, L33
Woosley, S. E., Heger, A., & Weaver, T. A. 2002, RvMP, 74, 1015